Toughening Linear Low-Density Polyethylene With Halloysite Nanotubes

Diego Pedrazzoli,[1] **Alessandro Pegoretti,**[1] **Ralf Thomann,**[2] **János Kristóf,**[3] **József Karger-Kocsis**[4,5]

[1]*Department of Industrial Engineering and INSTM Research Unit, University of Trento, via Sommarive 9, 38123 Trento, Italy*

[2]*Institut für Makromolekulare Chemie und Freiburger Materialforschungszentrum, Albert-Ludwigs-Universität Freiburg, Stefan-Meier-Str. 31, 79104 Freiburg, Germany*

[3]*Department of Analytical Chemistry, University of Pannonia, 8200 Veszprém, Hungary*

[4]*Faculty of Mechanical Engineering, Department of Polymer Engineering, Budapest University of Technology and Economics, Müegyetem rkp. 7-9, 1111 Budapest, Hungary*

[5]*MTA–BME Research Group for Composite Science and Technology, Budapest University of Technology and Economics, Müegyetem rkp. 3, 1111 Budapest, Hungary*

Linear low-density polyethylene (LLDPE)-based composites were prepared through melt compounding and hot pressing using both untreated and treated halloysite nanotubes (HNT) up to filler contents of 8 wt% to assess the role of the filler exfoliation and surface treatment on the thermal, mechanical, and rheological properties of the resulting composites. The addition of treated nanoparticles resulted in a better dispersion of the filler within the matrix, as confirmed by observations conducted at scanning and transmission electron microscopies. A decrease in both complex viscosity and shear storage modulus was recorded for all LLDPE-HNT nanocomposites in the molten state. Differential scanning calorimetry analysis evidenced that HNT addition produced an increase of the crystallization peak temperature, while thermogravimetric analysis showed a remarkable improvement of the thermal stability with the nanofiller content. The addition of treated HNT nanoparticles induced better improvements in elastic modulus and tensile properties at break without significant loss in ductility. The fracture toughness, evaluated by the essential work of fracture approach, showed remarkable improvements (up to a factor of 2) with addition of treated HNT. Conversely, incorporation of untreated HNT produced an adverse effect on the fracture toughness when considering the nanocomposite filled with 8 wt% HNT. Both creep tests and dynamic mechanical analyses showed an overall enhancement of the viscoelastic properties due to addition of HNT, revealing higher improvements in nanocomposites added with treated HNT. POLYM. COMPOS., 36:869–883, 2015. © 2014 Society of Plastics Engineers

INTRODUCTION

Increasing efforts have been devoted to the research of reinforced polymer composites exhibiting improved properties. In particular, while single-polymer composites are preferred for their low density and ultimate recycling [1], polymer nanocomposites have been recently attracted attention because of their novel and multifunctional properties [2]. Specifically, reinforcing thermoplastic polymers with nanotubes or nanoplatelets to form nanocomposites is a way to extend the usage of polymeric materials in engineering applications by improving their mechanical properties, namely elastic modulus and yield stress with filler contents as low as 5–10 wt% [3, 4]. Furthermore, filler's shape, dimension, aspect ratio, and surface characteristics play a key role in determining the morphology, and thus, the thermo-mechanical, rheological, flame resistance, and optical properties of the final composite [5, 6]. In particular, nanofillers such as carbon nanotubes (CNTs) [7–10], nanoclay [especially montmorillonite (MMT) 11–14], and expanded graphite nanoplatelets (xGnPs) [15–17] have attracted great attention in the past decades for the production of nanocomposites based on engineered polymers such as polypropylene (PP),

polyethylenes (PEs), polyamide (PA), rubbers, and epoxy resins [18–27].

Nonetheless, most of the reported literature indicate that there is a significant reduction in the elongation at break and/or impact strength in these materials when a nanofiller is added and when its content increases [26, 28]. Consequently, the use of nanocomposites may be limited by the losses in toughness. Conversely, nanofillers such as halloysite nanotubes (HNTs) makes it possible, contrary to other nanofillers, to significantly reduce the ductility loss on addition in a ductile matrix (e.g., PP [29] or PA6 [20]). Moreover, the addition of HNT, event at high content, has a moderate effect on the flow behavior of the polymer which can still be processed as the neat material [30, 31]. Halloysite is a kind of clay aluminosilicate mineral with hollow nanotubular structure mined from natural deposits. Chemically similar to kaolin, halloysite has a molecular formula of $Al_2Si_2O_5(OH)_4 \cdot nH_2O$ with 1:1 layer. Nanotubular geometry of halloysites exhibits nanoscale dimensions, with a typical length in the range of 0.1–15 μm, inner diameter of 5–30 nm, and outer diameter of 30–70 nm, depending on the deposits [32]. Various features of HNTs like rigidity, high aspect ratio, and low density of surface hydroxyl groups compared with other silicates, make it a promising reinforcing filler for polymer materials. Furthermore, its abundant availability, biocompatibility, and low price promoted HNTs as subject of recent research. When compared with CNTs, the naturally occurring HNTs are much cheaper and easily available. In particular, HNTs have high-mechanical strength and modulus and these features make it an ideal material for the fabrication of high-performance polymer nanocomposites [33]. Recently, HNTs are being attempted to be used as nanofiller in conjunction with various polymers such as PP, PA, rubber, and epoxy resin generally for strengthening and toughening of the matrix, but also to improve their thermal stability and flame retardancy and to reduce the coefficient of thermal expansion [33, 34]. Several different approaches and techniques have been utilized to realize nanocomposites with unique structures and desired performance [35].

It is expected that HNTs could be dispersed relatively uniformly in thermoplastics by direct melt blending, especially for polymers with high polarity such as PAs. Nevertheless, compatibilization between polyolefins and inorganics is challenging due to the great polarity discrepancy and the chemical inertness of the polyolefins. To increase the compatibility between PP and HNTs, Du et al. proposed a two-step method of grafting PP chains onto the surface of HNTs [36]. Modifications at the surfaces of HNTs provide an opportunity to expand the basal spacing of HNTs through intercalation of inorganic and organic compounds in their internal layers. This contributes to a better and more homogeneous dispersion of HNTs within the corresponding polymer during melt blending. Furthermore, the surface modification can remarkably enhance the wettability of the filler and adhesion between filler and matrix [37].

HNTs in various concentrations (5–30%) were used for preparing nanocomposites based on PA6 by simple melt extrusion process. It was found that HNTs influenced the fire performance of the composites, by developing thermal insulation barrier at their surface during burning. Nevertheless, relatively high concentrations of additive (15 wt%) are required to achieve the adequate level of fire retardancy similar to nanoclay additives [38].

Linear low-density polyethylene (LLDPE) is an important thermoplastic for the applications such as electric wire, cable, film, pipe, and container [39]. However, its applications are limited, especially due to its relatively low strength, low softening point, and flammability resistance. Therefore, it is opportune to modify LLDPE with the incorporation of nanofillers to get improved mechanical properties, flame retardancy as well as thermal stability [40–43]. Furthermore, both thermal and mechanical properties can be further enhanced by the addition of graft copolymers [44] which improve the dispersion degree of the filler and interface properties between filler and matrix.

The effects of HNTs on the flame retardancy of LLDPE were studied by Jia et al., with the results suggesting that HNTs are expected to be promising flame-retardant additives for LLDPE [44]. Moreover, Dorigato et al. studied the role of fumed silica nanoparticles, having different surface area and surface treatments, on the fracture behavior of LLDPE matrix through the essential work of fracture (EWF) method. The cited authors found prominent increments in both the initiation and the propagation terms of the specific work of fracture [45].

Researchers have recently focused on the study of the fracture toughness of a wide range of polymeric nanocomposites adopting the EWF method [46–48], because of its simple specimens' preparation, easy testing, and simple data reduction procedure [49]. In one of our previous work, we attempted to investigate the fracture toughness of LLDPE-boehmite alumina (BA) nanocomposites through EWF method, observing a toughness enhancement effect due to the nanofiller incorporation, but no particular dependence on the BA crystallite size and surface functionalization [50]. To the best of our knowledge, only few papers addressed the study of the effect of HNTs loading on the toughening mechanism of thermoplastic nanocomposites through the EWF method [20].

The present work aims at highlighting the enhancing effect of HNTs addition on the thermo-mechanical and rheological properties of LLDPE. Particular emphasis has been devoted to assess the fracture behavior evaluated by the EWF approach.

EXPERIMENTAL SECTION

Materials and Samples Preparation

The matrix used in this work was Flexirene® CL10 linear low-density polyethylene (MFI at 190°C and 2.16 kg = 2.6 g/10', Mn = 27000 g mol^{-1}, density = 0.918 g

TABLE 1. Physical properties of HNTs utilized in this work.

Filler	Density[a] (g cm^{-3})	BET surface area[b] (m^2 g^{-1})	$2\theta_{001}$[c] (°)	d_{001} (nm)	$2\theta_{020}$[c] (°)	d_{020} (nm)	$2\theta_{002}$[c] (°)	d_{002} (nm)
uHNT	2.206 ± 0.001	31.3	13.26	0.667	20.43	0.434	24.71	0.360
tHNT	1.700 ± 0.001	61.8	12.41	0.713	20.29	0.437	24.90	0.357

[a]Measurements were performed by using a Micromeritics Accupyc® 1330 helium pycnometer ($T = 23°C$).
[b]Brunauer–Emett–Teller specific surface area [51].
[c]Reflection ($2\theta_{hkl}$) and basal spacing (d_{hkl}) relative to XRD analyses.

cm^{-3}, glass transition temperature = $-110.5°C$), produced by Polimeri Europa S.p.A., now Versalis (Mantova, Italy) using Ziegler–Natta catalysis and butene as a comonomer (C$_4$-LLDPE). This type of LLDPE is suitable for cast extrusion of thin film with high optical properties.

Untreated HNT (uHNT) were mined from Turplu/Balikesir (Turkey) and presented an oxide composition as follows (wt/wt%): SiO$_2$ (46.7%), Al$_2$O$_3$ (33.1%), Fe$_2$O$_3$ (2.96%), CaO (0.37%), MgO (0.26%), Na$_2$O (0.12%), K$_2$O (0.27%), TiO$_2$ (0.03%). Noteworthy, uHNT presented a very limited amount of kaolinite and can be considered as pure HNTs. Treated HNT (tHNT) were mined from Szegilong (Hungary) and presented a different composition, morphology, and surface properties due to a chemical treatment of the initial HNT. In particular, a significant amount of kaolinite was present in the HNT. tHNT presented the following oxide composition (wt/wt%): SiO$_2$ (46.7%), Al$_2$O$_3$ (33.9%), Fe$_2$O$_3$ (3.21%), CaO (0.55%), MgO (0.15%), Na$_2$O (0.10%), K$_2$O (0.22%), TiO$_2$ (0.06%).

The preparation of tHNT can be described as follows: intercalation with K-acetate (CH$_3$CO$_2$K; 30:70 wt% K-acetate/wt% HNT), drying ($T = 110°C$, $t = 24$ h), treatment with ethylene glycol (C$_2$H$_6$O$_2$; 5:1 mol ethylene glycol/mol HNT, $T = 150°C$, $t = 4$ h), and final treatment with n-hexylamine (C$_6$H$_{15}$N; 5:1 mol n-hexylamine/mol HNT, $T = 20°C$, $t = 48$ h). After each step, the degree of intercalation was determined by X-ray diffraction (XRD). Generally, complete delamination was achieved when the last step (treatment with hexylamine) was repeated one more time. The excess reagents were removed from the particles' surface after each step with washing with acetone (using a G4-type filter). After the last step, excess reagent was removed by drying at 50°C for 2 h. Untreated and tHNT were chosen on purpose from different origins to compare pure halloysite with natural halloysite (i.e., halloysite containing kaoline), respectively.

Table 1 summarizes the experimental density, Brunauer–Emett–Teller specific surface area and the diffraction pattern characteristics of the HNTs used in this work.

LLDPE was used as received while the fillers were dried at 80°C for 12 h prior to use. The samples were prepared by melt compounding in a Brabender® Plasti-Corder internal mixer ($T = 170°C$, $n = 50$ rpm, $t = 15$ min) followed by compression moulding using a Collin® P200E hot press ($T = 170°C$, $p = 2$ MPa, $t = 15$ min), to get plane sheets with thickness of around 0.5 mm. The filler content was varied between 0 and 8 wt%.

The unfilled matrix was denoted as LLDPE, while nanocomposites were designated indicating the matrix, the filler type and the filler weight amount. For instance, a sample filled with 4 wt% of uHNT is indicated as LLDPE-uHNT-4.

Experimental Techniques

Filler Characterization. Density measurements were carried out through helium pycnometry technique (Micromeritics® Accupyc 1330 helium pycnometer, Norcross), at a temperature of 23°C, using a testing chamber of 3.5 cm^3.

XRD analyses were performed through a Rigaku® 3D Max X-ray diffractometer, scanning the samples in a 2θ range between 3 and 67°, at a 2θ step of 0.1°. The wavelength of the X-ray source was 0.15418 nm.

To evaluate the morphological features of HNTs, transmission electron microscope (TEM) micrographs were taken through a Philips® CM12 TEM adopting an acceleration voltage of 120 kV. The powder samples used for the observations were dispersed in a solution of acetone and sonicated for 5 min prior to observations.

Nanocomposite Characterization. *Electron Microscopy and Spectroscopy Analyses.* The dispersion state of the HNT particles in the LLDPE matrix was studied by both scanning electron microscopy (SEM) using a FEI Quanta 250 FEG device (FEI, Hillsboro, Oregon) and by TEM on a Zeiss LEO 912 Omega device (Zeiss, Oberkochen, Germany). Thin specimens (ca. 50 nm) were cryomicrotomed with a Diatome diamond knife at $T = -120°C$ using a Leica Ultracut UCT / EM FCS ultramicrotome equipped with a cryo-chamber. The cryocut surfaces of the specimens were inspected in SEM (acceleration voltage 10 kV) without sputtering, using a high resolution vCD detector for backscattered electrons. XRD analyses were performed on nanocomposite samples using the same testing conditions as for the filler characterization. IR spectroscopic study was carried out on 80-μm thick nanocomposite films within a scanning interval between 650 and 4000 cm^{-1}, setting a resolution of 2 cm^{-1} for a total number of 64 coadded scans.

Rheology Measurements. The melt rheology of the nanocomposites was analyzed by an Rheoplus 32 V3 dynamic oscillatory rheometer (Anton Paar Physics, Ostfildern, Germany) working under controlled strain conditions. The test geometry was cone-plate (cone angle = 1°) with a cone diameter of 25 mm, and the tests were performed on compression moulded disks of around 0.6 mm thickness. The thickness of the gap was set at 0.5 mm by squeezing the initial LLDPE disk. Frequency sweep tests were carried out at $T = 180°C$. During the measurements, a small amplitude (1%) oscillatory shear was applied to the samples. The storage and loss shear moduli (G' and G'', respectively) and the dynamic viscosity $|\eta^*|$ were measured as a function of angular frequency (ω) in the range 0.01–100 rad/s.

Thermal Analyses. Differential scanning calorimetry (DSC) tests were carried out by a Mettler® DSC30 apparatus (Schwerzenbach, Switzerland) under a constant nitrogen flow of 100 ml min^{-1}. The samples were heated up to 200°C at a rate of 10°C min^{-1} with subsequent crystallization test down to 0°C, at a cooling rate of 10°C min^{-1}. A subsequent heating scan was performed at 10°C min^{-1}. The melting enthalpy of 100% crystalline PE has been considered as $\Delta H^0 = 290$ J g^{-1} [52]. Moreover, the crystallinity χ_c of nanocomposite samples was calculated by taking the weight fraction of LLDPE in the composite into account. The melting temperatures T_{m1} and T_{m2} were recorded during the first and second heating scan, respectively. The crystallization enthalpy ΔH_c was measured by integrating the heat flow curve registered during cooling.

Thermogravimetric analyses (TGA) were carried out through a Q5000 IR thermogravimetric analyzer (TA Instruments-Waters LLC, New Castle) imposing a temperature ramp between 40 and 700°C at a heating rate of 10°C min^{-1} under a constant nitrogen flow of 25 ml min^{-1}. The onset of degradation temperature ($T_{d,onset}$) was determined by the point of intersection of tangents to two branches of the thermogravimetric curve, while the maximum rate of degradation temperature ($T_{d,max}$) was determined from the peak maxima in the first derivative of weight loss curve. Furthermore, the maximum mass loss rate (MMLR) was also recorded at $T_{d,max}$.

Mechanical Tests. Uniaxial tensile tests were performed with an Instron® 4502 (Norwood) tensile machine on samples of at least five ISO 527 type 1BA specimens. The tests were carried out at a crosshead speed of 0.25 mm min^{-1} up to a maximum axial deformation of 1%. The strain was recorded using a resistance extensometer Instron® model 2620-601 with a gage length of 12.5 mm. According to ISO 527 standard, the elastic modulus was measured as a secant value between deformation levels of 0.05 and 0.25%. Uniaxial tensile properties, such as stress at yield (σ_y), stress at break (σ_b), and strain at break (ε_b) were determined at a higher crosshead speed (50 mm min^{-1}) without extensometer.

Creep tests were performed in tensile mode on a dynamic mechanical analyzer DMA Q800 (TA Instruments®-Waters LLC, New Castle) applying a constant stress (σ_0) of 1 MPa (i.e., about 10% of the stress at yield of unfilled LLDPE) for 3600 s at 30°C. Rectangular specimens, 25-mm long, 5-mm wide, and 0.5-mm thick, were used whereby setting a gage length of 11.5 mm. The creep compliance $D(t)$, computed as the ratio between the strain and the creep stress, was plotted against the time.

Dynamic mechanical thermal analysis (DMTA) measurements were carried out in tensile mode by a DMA Q800 testing machine (TA Instruments®-Waters LLC) on strips 25-mm long, 5-mm wide, and 0.5-mm thick. The samples were analyzed over a temperature range from −130 to 80°C, at a heating rate of 3°C min^{-1} and a frequency of 1 Hz. A preload of 0.2 MPa and a maximum strain of 0.05% were set for each test.

The toughening mechanism associated to the presence of HNT nanotubes in LLDPE was assessed through the essential work of fracture (EWF) method under tensile conditions. According to this methodology [53], the total fracture energy (W_f) spent to bring a precracked body to complete failure can be partitioned into a work (W_e) required to create new fracture surfaces and, therefore, essential for the fracture process and a nonessential work (W_p) dissipated for the plastic deformation of the outer plastic zone. Under plane-stress conditions, W_e is proportional to the ligament length of the sample (L), whereas the nonessential work of fracture is proportional to L^2.

Therefore,

$$W_f = W_e + W_p = w_f LB = w_e LB + w_p \beta L^2 B \qquad (1)$$

which can be expressed in specific terms normalizing by the ligament area (LB) as

$$w_f = w_e + \beta w_p L \qquad (2)$$

where B is the specimen thickness, β is a shape factor depending on both the material and the geometry of the body, w_e is the specific essential work of fracture, and w_p is the specific nonessential work of fracture. The quantities w_e and βw_p are determined by a linear interpolation of a series of experimental data of w_f obtained by testing specimens having different ligament lengths. The quantity w_p can be explicitly deduced for some shapes of the outer plastic zone with known β, for example, for circular, elliptical, and diamond-type zones β is given by $\pi/4$, $\pi h/4L$, and $h/2L$, respectively, where h is the height of the corresponding zone [49].

Furthermore, the specific total work of fracture (w_f) can be divided into specific work of fracture for yielding (w_y) and specific work of necking (w_n; [49] and references therein):

$$w_f = w_y + w_n = \left(w_{e,y} + \beta' w_{p,y} L \right) + \left(w_{e,n} + \beta'' w_{p,n} L \right). \qquad (3)$$

DEN-T specimens (width 30 mm, height 80 mm, thickness 0.5 mm, distance between the grips 50 mm) were tested with an Instron® 4502 (Norwood) tensile machine. At least four tests were conducted for every
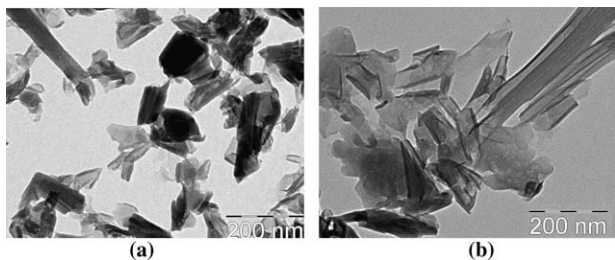
FIG. 1. TEM micrographs of (a) uHNT and (b) tHNT.

ligament length, and five different ligament lengths between 5 and 13 mm were tested setting a crosshead speed of 10 mm min^{-1}. The notches were introduced using a home made apparatus mounting a razor blade, to obtain a very sharp crack tip. From SEM images, it was possible to estimate an average crack tip radius of less than 20 μm. The exact ligament lengths were measured with a profile projector with an accuracy of 0.01 mm.

To study the fracture behavior of the material at high strain rate levels, tensile impact tests were carried out with a CEAST® (Norwood) tensile impact instrumented pendulum. The striker, with a mass of 3.65 kg and an initial angular position of 63°, had an impact speed of 2 m s^{-1} and a total impact energy of 7.3 J. The specific tensile energy to break (TEB), obtained by integrating load-displacement curves, was obtained by applying *Eq. 4*.

$$\text{TEB} = \frac{1}{A}\left[V_0 \int_0^{tr} F\,dt - \frac{1}{2m}\left[\int_0^{tr} F\,dt\right]^2\right] \qquad (4)$$

where A is the cross section of the specimen, m is the striker mass, tr is the time to rupture and V_0 is the impact speed.

RESULTS AND DISCUSSION

Morphology of HNT and LLDPE/HNT Nanocomposites

The morphological characteristics of uHNT and tHNT were obtained from the TEM micrographs depicted in Fig. 1a and b, respectively. Firstly, it is worth mentioning that HNT mined from different sources can vary in the level of hydration, morphology (dimension of inner and outer diameter, length and aspect ratio) and color, depending on the substitutional metals and on mineral origin [37]. uHNT was present in a high proportion of thick unexfoliated stacks, few platy particles, and very short tubes. Conversely, the effect of the exfoliation promoted by chemical treatment is observable in the case of tHNT, mainly represented by platy particles and more and longer tubular elements, with an electron-transparent central lumen.

In particular, the tubular particles showed dimensions within the ranges of outer diameter 30–60 nm, inner diameter 6–20 nm, and length 150 nm–2 μm. The thickness of the HNT wall is around 5–25 nm. TEM micrographs indicate that although uHNT and tHNT show different exfoliation and dispersion, their structure and size are comparable, confirming that the two fillers can be used to investigate the solely effect of the surface treatment on the properties of LLDPE.

The density values measured through helium pycnometry on the two HNTs are reported in Table 1. In particular, tHNT presents a density 23% lower with respect to uHNT, clearly indicating a higher degree of exfoliation and dispersion of the tHNT particles due to chemical treatment, as confirmed by TEM observations.

Cryocut sections of composites were examined through SEM and TEM analysis. In particular, SEM pictures taken from the cryocut surfaces of LLDPE composites with 4 and 8 wt% tHNT are represented in Fig. 2a and b. It is evident from the SEM microphotographs of LLDPE-tHNT that the nanotubes are finely and homogeneously dispersed within the matrix even at 8 wt% filler loading. The observations of good dispersion are consistent with the mechanical performance improvement reported later. The poor dispersion of uHNT resulting in numerous and big agglomerates is clearly observable also by naked eye. For this reason, the SEM and TEM micrographs of LLDPE-uHNT composites are not reported.
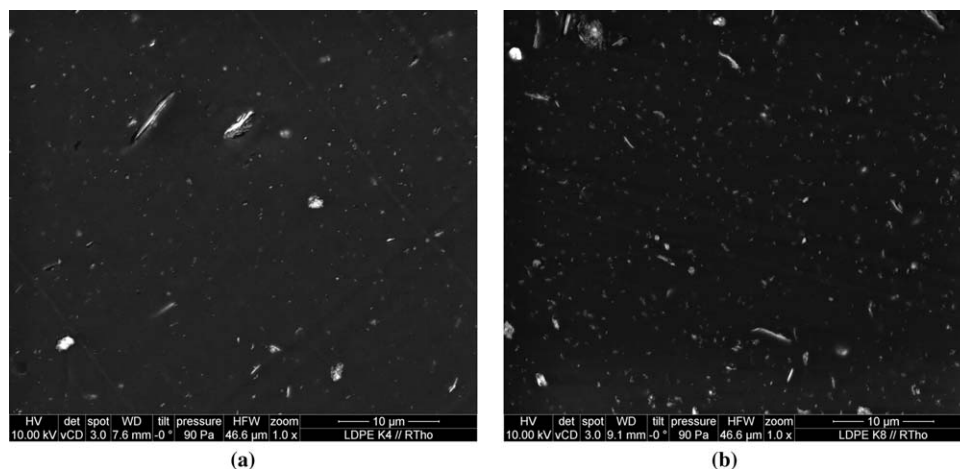
FIG. 2. SEM images of the cryocut surfaces of (a) LLDPE-tHNT-4 and (b) LLDPE-tHNT-8.
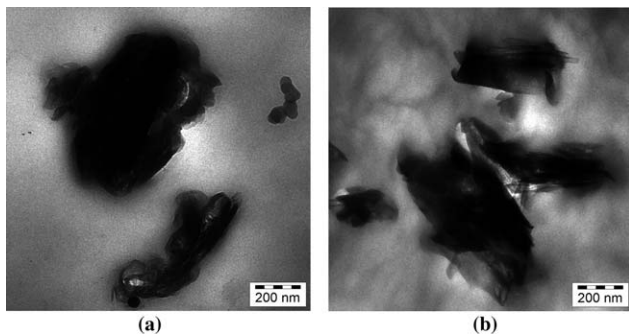
FIG. 3. TEM micrographs of the cryocut surfaces of (a) LLDPE-tHNT-4 and (b) LLDPE-tHNT-8 nanocomposites.

TEM pictures confirm that the designation nanocomposite is correctly used (Fig. 3a and b) in the case of LLDPE-tHNT composites. Both SEM and TEM morphological analysis confirm that tHNT can be finely dispersed within the LLDPE matrix even at high filler contents and without using polymeric compatibilizer, while uHNT tends to form micrometric aggregates and agglomerates producing negative effects on the mechanical properties.

XRD diffractograms of the tHNT and uHNT are displayed in Fig. 4a. The most relevant values of 2θ and their relative basal spacing are also presented in Table 1. In particular, tHNT and uHNT show a small reflection at $2\theta_{001,t} = 12.41°$ and $2\theta_{001,u} = 13.26°$, respectively, which is related to the <001> crystallographic plane. The correspondent basal spacing is equal to 0.713 and 0.667 nm, respectively, confirming the multiwall nanotubular structures at nanoscale of HNT. Furthermore, the difference found in the basal spacings suggests that exfoliation occurred in tHNT owing to the chemical treatment used.

Other relevant reflections are located at higher values of 2θ, corresponding to the <020> and <002> crystallographic planes. Interestingly, no significant difference can be noticed between the XRD spectra of tHNT and uHNT.
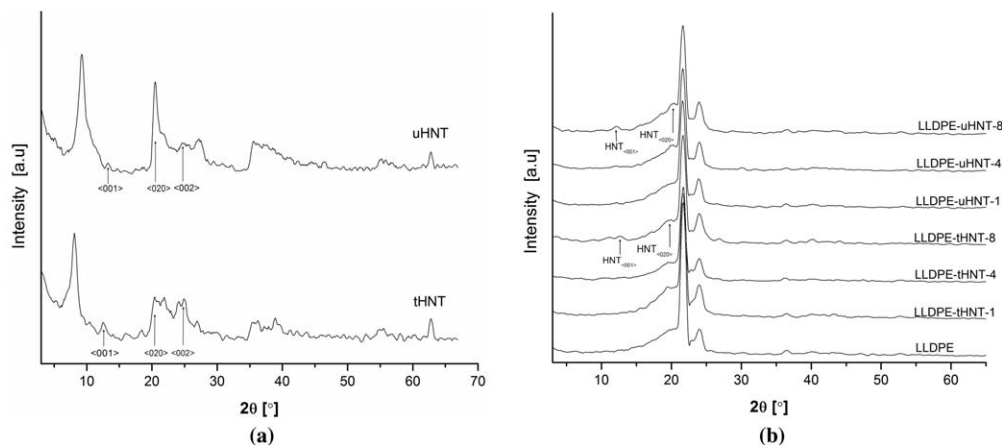
According to XRD diffractograms of LLDPE nanocomposites, the intensity of the signals of all HNT characteristic peaks slightly increases with the nanofiller amount and becomes well recognizable in the diffractograms of composites with 8 wt% HNT (Fig. 4b). These peaks confirm the presence of structures with limited intercalation and can be attributed to the formation of nanocomposites. Nevertheless, both reflections of HNT at around $2\theta = 20.4°$ and $2\theta = 24.7°$ are overlapped by characteristic LLDPE reflections and it is difficult to estimate an amplitude increase dependent on the nanofiller type and amount.

Representative IR spectra of the unfilled LLDPE and corresponding nanocomposites with tHNT and uHNT are plotted for comparison in Fig. 5a and b, respectively. Furthermore, the IR spectra of the HNT nanopowders are included in the correspondent plots. Most of the peaks recognizable in the IR spectrum of tHNT nanopowder correspond to those reported in the literature [54–56]. In particular, the bands at 797 and 755 cm^{-1} are assigned to translational vibrations of the external OH groups as well as out-of-plane OH bending, while the peak at 695 cm^{-1} is related to the perpendicular Si—O stretching bond. The absorption bands nearby 1092 and 1030 cm^{-1} are assigned to stretching vibration of Si—O bonds, while the characteristic absorption band at 912 cm^{-1} is due to flexural vibrations of Al—OH. The results confirm coexistence of hydroxyl groups and Si—O bonds on the surfaces of HNTs.

The peak at 1327 cm^{-1} is associated to CH$_3$ deformation. The absorption peaks at 1558 and 1467 cm^{-1} are assigned to C=O antisymmetric and symmetric stretching vibrations, respectively, while the peaks located at 2956, 2926, and 2857 cm^{-1} are attributed to C—H stretch vibrations [57].

The absorption band at 3622 cm^{-1} is the characteristic absorption of hydroxyl groups located on shared interfaces of layered structure consisting of silicon-oxygen tetrahedron and aluminium-oxygen octahedron, and the band at 3694 cm^{-1} is the characteristic absorption of external

FIG. 4. XRD traces of (a) HNT nanopowders, and (b) LLDPE and its HNT nanocomposites.
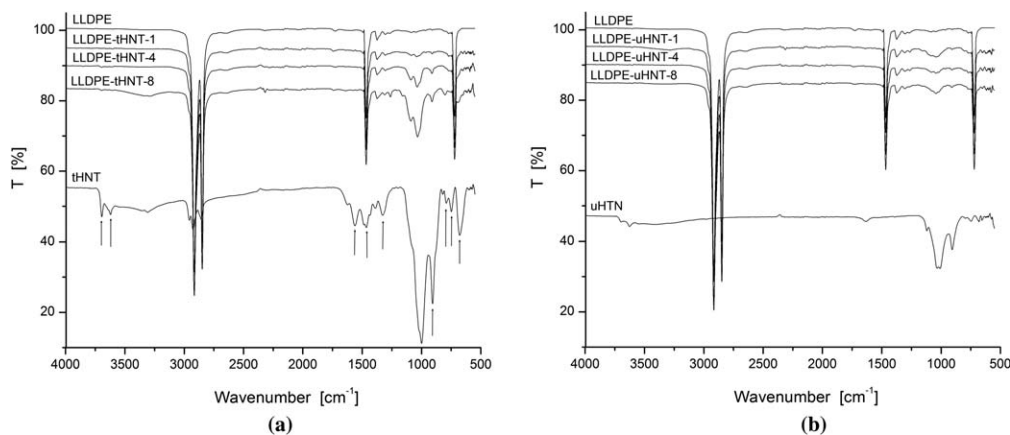
FIG. 5. FTIR spectra of (a) tHNT nanopowder and LLDPE-tHNT nanocomposites and (b) uHNT nanopowder and LLDPE-uHNT nanocomposites.

hydroxyl groups located on nonshared surfaces of the layered structure [44].

When considering the IR spectrum of uHNT, it is noticeable that the characteristic peaks attributable to the K-acetate and hexylamine located within the bands 1327–1558 and 2857–2956 cm^{-1} are absent, while the typical peaks of HNT are mostly reduced or suppressed. In particular, limited peaks are observable at 3622 and 3694 cm^{-1}, indicating a lower density of inner surface hydroxyl groups. Moreover, the bands at 695, 755, and 797 cm^{-1} are also suppressed and thus appear as traces.

The spectra of LLDPE-tHNT nanocomposites present the characteristic peaks attributable to tHNT, whose intensity increases with the filler content. Conversely, no significant difference can be observed among the spectra of LLDPE-uHNT samples, clearly indicating a lower degree of chemical interaction between filler and matrix by contrast to the LLDPE-tHNT composites.

Rheological Behavior of LLDPE/HNT Nanocomposites

The effect of the filler addition on the isothermal frequency dependence of the dynamic shear storage modulus (G') and complex viscosity ($|\eta^*|$) is reported in Fig. 6a for

unfilled LLDPE and LLDPE composites filled with 4 wt% HNT. A general decrease in both G' and $|\eta^*|$ can be easily detected for all LLDPE-HNT-4 nanocomposites over the whole frequency range. A similar decrease of both G' and $|\eta^*|$ is also recorded in the case of composites filled with 8 wt% HNT (Fig. 6b). For both LLDPE-HNT-4 and LLDPE-HNT-8, practically no difference is observable as a function of the HNT types. Noteworthy, the lowering in viscosity is very beneficial for the material processing. Moreover, some deviations in the measured parameters can be observed at low frequencies, mainly with respect to the G' values. This experimental artifacts are most likely due to the adopted cone-plate configuration.

Incorporation of nanofillers in thermoplastics is generally associated with a marked increase in the melt viscosity, at least in the range of low frequencies. Furthermore, a prominent enhancement in G' is usually observed. These changes are normally assigned to a pseudo solid-like transition caused by the dispersed nanoparticles [58–64]. Nevertheless, the lowering of both $|\eta^*|$ and G' by HNT addition to LLDPE is opposed to that general trend. Khumalo et al. observed a similar rheological behavior in the case of PE filled with synthetic boehmite (BA)
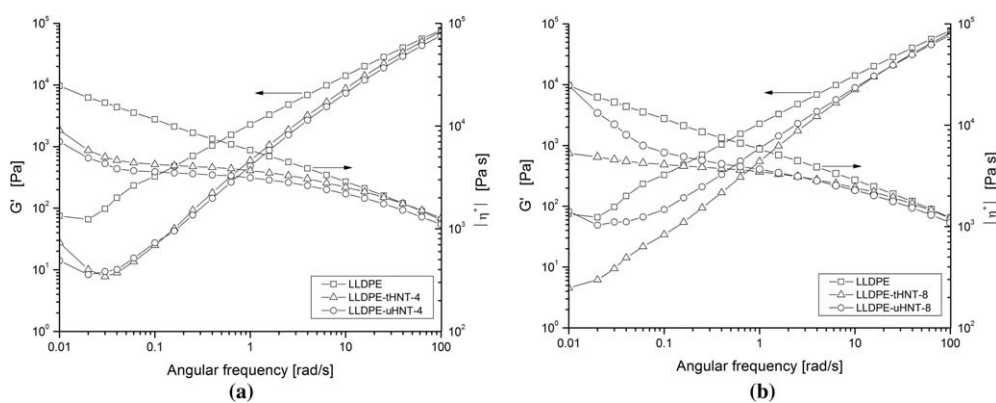
FIG. 6. Complex viscosity $|\eta^*|$ and storage modulus (G') as a function of angular frequency (ω) for (a) LLDPE and LLDPE-HNT-4 nanocomposites and (b) LLDPE and LLDPE-HNT-8 nanocomposites.

TABLE 2. Melting and crystallization characteristics of LLDPE and relative nanocomposites from DSC measurements.

Sample	T_{m1} (°C)	ΔH_{m1} (J/g)[χ_{m1} (%)]	T_c (°C)	ΔH_c (J/g)[χ_c (%)]	T_{m2} (°C)	ΔH_{m2} (J/g)[χ_{m2} (%)]
LLDPE	118.0	102.4 (35.3)	104.2	98.4 (33.9)	117.5	98.4 (33.9)
LLDPE-uHNT-1	117.8	101.3 (35.3)	105.5	101.0 (35.2)	117.7	100.3 (34.9)
LLDPE-uHNT-4	119.1	99.2 (35.6)	107.9	98.1 (35.2)	118.1	97.6 (35.1)
LLDPE-uHNT-8	119.1	96.5 (36.2)	107.1	94.9 (35.6)	117.9	94.0 (35.2)
LLDPE-tHNT-1	118.3	102.1 (35.6)	105.4	100.1 (34.9)	117.7	99.3 (34.6)
LLDPE-tHNT-4	118.2	99.5 (35.7)	108.2	97.9 (35.2)	117.9	97.2 (34.9)
LLDPE-tHNT-8	118.1	97.9 (36.7)	107.7	95.1 (35.6)	118.1	94.5 (35.4)

T_{m1}: Melting temperature recorded during the first heating scan.
ΔH_{m1} (χ_{m1}): Melting enthalpy and normalized crystallinity recorded during the first heating scan.
T_c: Crystallization peak temperature.
ΔH_c (χ_c): Crystallization enthalpy and normalized crystallinity.
T_{m2}: Melting temperature recorded during the second heating scan.
ΔH_{m2} (χ_{m2}): Melting enthalpy and normalized crystallinity recorded during the second heating scan.

nanocomposites [65]. In one of our previous works, we studied the rheological behavior of LLDPE nanocomposites added with BA and found that the addition of the filler produces a decrease in $|\eta^*|$ and G' compared to unfilled LLDPE [51]. Fernández et al. studied PA6 nanocomposites with HNT, observing a markedly lower viscosity in the molten nanocomposites up to a filler content as high as 30 wt% [31].

The viscosity decrease recorded in LLDPE nanocomposites might be ascribed to the morphology of the polymer chains. In fact, LLDPE is a highly branched polymer whose chains would tend to get entangled and apparently HNT particles can fill in the spaces between chain branches. This provides some "rigidity" enabling easier flow [30]. Moreover, an alignment of the HNT within the chain branches might also occur, resulting in an even greater rigidity effect. Nevertheless, future research is required to give further clarifications on the mechanisms of decrease in viscosity in polyolefins by HNT incorporation.

Thermal Properties of LLDPE/HNT Nanocomposites

The addition of both uHNT and tHNT produces a moderate increase of the crystallization temperature of LLDPE, but no particular dependence of nucleating effect on the HNT type is evidenced (Table 2). Furthermore, the crystallization temperature seems to approach a plateau for HNT content higher than 4 wt%.

The nucleating effect of HNT was already reported in previous papers regarding PA6 [36] and PP nanocomposites [66]. Interestingly, Liu et al. investigated isotactic PP filled with HNT and found HNT to have dual nucleating ability for α and β crystalline forms of PP under appropriate kinetics conditions [66]. It was also claimed that the formation of the β crystalline form in the PP composites is correlated to the unique surface characteristics of the HNT. Recently, Guo et al. studied the nonisothermal crystallization behavior and the polymorphism of PA6 and PA6/HNT nanocomposites [18]. It was found

that HNT acts as nucleating agent, accelerates the crystallization and induces the formation of γ-phase crystals. These results suggest that, similar to other nano-sized inorganic fillers, such as silica and MMT, HNTs serve as nucleating agents and promote polymorphism of the nanocomposites [35].

Concurrently, the melting temperature recorded during the second scan (T_{m2}) and the crystallinity (χ_c) are slightly higher in LLDPE nanocomposites, but do not seem to have a direct correlation with the nanofiller content. The increase in crystallinity occurring on nanomodification of LLDPE can be mainly attributed to the nucleating effect of the nanofiller. The higher crystallization temperature exhibited by LLDPE nanocomposites might indicate that the polymer chains have more time, at higher temperature, to rearrange and form more perfect and/or thicker crystals. However, a further determination of the crystallization induction time, defined as the time difference between onset and endset of nonisothermal crystallization, would be required to justify this hypothesis.

The thermal resistance parameters as detected in TGA measurements are reported in Table 3. When considering LLDPE-HNT nanocomposites, both $T_{d,onset}$ and $T_{d,max}$ markedly increase with the filler content, showing a slightly higher efficiency in LLDPE-tHNT samples. Improved thermal stability due to the addition of HNT has been already reported for PA6 [38] and PP [67] nanocomposites.

Interestingly, the char content recorded for LLDPE nanocomposites is markedly lower than the added amount of filler, indicating that the filler experienced weight loss during heating. This is probably due to the release of crystal water in the range between 430 and 570°C [44]. In particular, the lower char content observed in tHNT with respect to uHNT can be attributed to two main causes: the degradation and further loss of the functional groups derived from the chemical treatment of tHNT and the possible higher content of crystal water in tHNT.

Exposing the specimen to elevated temperatures may induce filler aggregates to agglomerate on the surface of

TABLE 3. TGA parameters of LLDPE and relative nanocomposites.

Sample	$T_{d,onset}$ (°C)	$T_{d,max}$ (°C)	MMLR (mg°C^{-1})	Char (%)
LLDPE	457.0	477.1	0.195	0.3
LLDPE-uHNT-1	458.9	478.0	0.221	0.6
LLDPE-uHNT-4	461.5	478.2	0.243	2.6
LLDPE-uHNT-8	465.3	480.4	0.293	5.7
LLDPE-tHNT-1	458.5	480.8	0.236	0.4
LLDPE-tHNT-4	461.7	482.2	0.272	1.8
LLDPE-tHNT-8	465.7	484.2	0.308	5.0
uHNT	–	–	–	74.7
tHNT	–	–	–	57.9

$T_{d,onset}$: Onset degradation temperature.
$T_{d,max}$: Maximum degradation rate temperature.
MMLR: Maximum mass loss rate.
Char (%): Residual weight percentage.

the molten polymer, thus, creating a barrier that physically protects the rest of the polymer and hinders the volatilization of the oligomers generated during the combustion process [68]. Thus, in general, the higher the filler amount the lower the MMLR. However, this is not the case, as a higher content of HNT is associated to a greater MMLR (Table 3). In fact, the filler weight loss increases with the HNT content and this effect is probably preponderant on the MMLR decrease due to creation of physical barrier by filler aggregates.

Mechanical Properties of LLDPE/HNT Nanocomposites

As reported in Table 4, the addition of HNT nanoparticles produces a significant increase of the elastic modulus of the LLDPE matrix, showing a higher efficiency in the case of tHNT. In particular, an improvement of 94% is reached for systems filled with 8 wt% of tHNT, compared to unfilled LLDPE.

The reinforcing effect provided by nanofiller incorporation is most often explained by the formation of an interphase region between the matrix and the particles. It has also been demonstrated that nanoparticles agglomeration is another significant mechanism responsible for stiffness increases in polymer nanocomposites [69]. A recent approach, developed by Dorigato et al. [43], was adopted to model the elastic modulus of LLDPE-HNT nanocomposites taking into account the stiffening effect provided by nanoparticles composed of primary aggregates and agglomerates. Note that the hypothesis behind this model is that part of the polymer matrix is mechanically constrained within the aggregates and agglomerates [43]. To implement the model, the Poisson's ratio of matrix and filler were chosen as 0.44 and 0.22, respectively, while the elastic modulus of filler was set to 300 GPa in according to literature data [70, 71].

The relative elastic modulus of the LLDPE-HNT composites is plotted in Fig. 7 as a function of the filler volume fraction, along with the fitting curves obtained with the adopted model. It can be noticed that the proposed model can model very well the elastic modulus of LLDPE-tHNT-x and LLDPE-uHNT-x composites over the whole range of filler concentration. Furthermore, the significant increase of the elastic modulus detected for nanocomposites is associated to elevated α values, which depends on the fraction of matrix constrained by nanoparticles [43]. As already noticed by Dorigato et al. when applying the model in the case of LLDPE filled with fumed silica nanoparticles, an apparent correlation exists between the α parameter and filler surface area [43] (Table 1). Specifically, tHNT possesses greater surface area than uHNT due to higher exfoliation, indicating higher capability of being intercalated by polymer matrix during compounding, with a consequent greater fraction of matrix constrained by nanoparticles' agglomerates.

Both yield stress and stress at break decrease with the filler content in the case of LLDPE-uHNT nanocomposites, probably because of extensive filler aggregation [28]. For the same reason, the elongation at break is lower than that of unfilled LLDPE. The increasing brittleness of the composites with filler content was also revealed by the tensile energy at break recorded during quasi-static tensile tests (TEB$_{qs}$). In particular, the presence of HNT particles causes stress concentration. Furthermore, interfacial failure might be more pronounced with increasing loading of halloysite.

The yield stress appears slightly higher in LLDPE-tHNT composites with respect to LLDPE, while stress at break and elongation at break moderately decrease, showing a stiffening effect which only slightly reduces the matrix ductility up to a filler content of 8 wt%. Similar

TABLE 4. Quasi-static tensile properties at yield and at break.

Sample	Tensile modulus (MPa)	Tensile stress at yield (MPa)	Tensile stress at break (MPa)	Elongation at break (%)	TEB$_{qs}$[a] (J/m^3)
LLDPE	200 ± 6	11.7 ± 0.2	21.6 ± 1.0	1390 ± 91	183.5 ± 14.1
LLDPE-uHNT-1	216 ± 13	11.2 ± 0.8	19.4 ± 0.8	1085 ± 58	172.1 ± 17.3
LLDPE-uHNT-4	248 ± 17	10.8 ± 0.4	13.7 ± 0.6	851 ± 74	160.5 ± 16.2
LLDPE-uHNT-8	322 ± 5	11.6 ± 0.4	13.8 ± 0.7	713 ± 26	151.2 ± 14.9
LLDPE-tHNT-1	220 ± 16	12.8 ± 0.2	21.0 ± 0.6	1157 ± 66	176.2 ± 15.2
LLDPE-tHNT-4	284 ± 24	13.8 ± 0.3	18.8 ± 0.4	1001 ± 19	173.5 ± 14.1
LLDPE-tHNT-8	388 ± 46	12.6 ± 0.3	18.9 ± 0.3	1017 ± 45	174.2 ± 16.3

[a]Tensile energy to break measured during quasi-static tensile mechanical test.
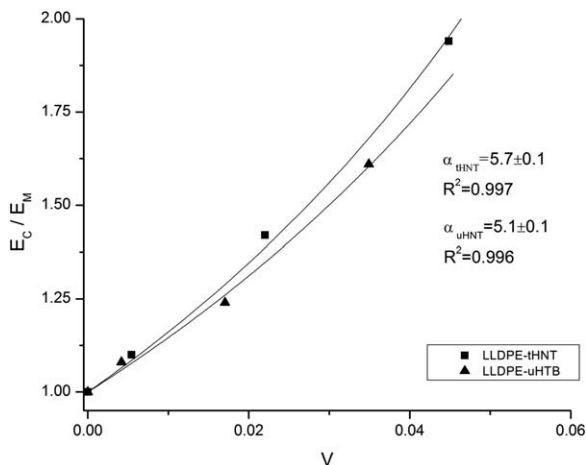
FIG. 7. Relative elastic modulus (E_C/E_M, where C and M subscripts refer to the composite and matrix, respectively) of LLDPE-HNT nanocomposites as a function of the filler volume content (V). Fitting of experimental data according to the model proposed by Dorigato et al. [42] (continuous line). Note that the error bars of experimental data are not given for sake of clarity.

behavior at yield and at break was found for PA6-HNT nanocomposites [35] and for PP-HNT samples [20].

In Fig. 8 the isothermal creep compliance of unfilled LLDPE and composites added with 4 and 8 wt% HNT, under a constant load of 1 MPa and at 30°C, is reported, whereas in Table 5, the elastic (D_e) and total components of the creep compliance after 2000 s ($D_{tot,2000}$) are summarized. The introduction of HNTs leads to a significant improvement of the creep stability of the material. It is generally believed that nanoparticles can effectively restrict the motion of polymer chains, influencing the stress transfer at a nanoscale, with positive effects on the creep resistance of the material [72]. Furthermore, tHNTs are more efficient than uHNTs in reducing the creep compliance, probably due to the better restriction of molecular chains during the viscous flow, showing a dependence on the HNT surface area and exfoliation.

The storage modulus (E') increases markedly with increasing HNT content, probably due to the restrictions of the molecular chains motion (Table 5), indicating that the incorporation of HNT nanoparticles remarkably enhances stiffness and load bearing capability of the material. As already seen in the case of tensile properties and creep resistance, the addition of tHNT produces the highest improvement in E'. The enhancement of the thermo-mechanical properties can be attributed to three factors: the high intrinsic stiffness of the nanotubes resulting from their tubular structure, the interaction between filler and matrix and their good dispersion within the matrix [19]. However, only the first two factors seem to be responsible for the increased modulus in LLDPE-uHNT nanocomposites, whereas the third factor may contribute in the case of LLDPE-tHNT, which is in line with SEM observations.

The loss modulus (E'') increases remarkably with increasing HNT content, without a clear dependence on

the HNT type. The glass transition temperature (T_g), as extrapolated from the tan δ peak, was slightly higher for all nanocomposites with respect to unfilled LLDPE. In particular, the addition of HNTs into the LLDPE matrix may have two opposite effects on the T_g of the polymer: (i) a T_g decrease associated to the reduced entanglements and interactions among LLDPE chains due to the presence of the nanotubes whereby enhancing the motion of the polymer chains and (ii) a T_g increase caused by a restriction of the segmental motion of LLDPE chains located near the nanotubes' surface in the interphase region [19].

In the LLDPE-uHNT nanocomposites, the HNTs might reduce the intermolecular interactions among LLDPE chains and thus the T_g reduction dominates. However, above 4 wt% HNTs, this effect is compensated by the interactions between HNTs and LLDPE chains. Therefore, T_g shifts to slightly higher temperatures. Conversely, in LLDPE-tHNT nanocomposites, the restriction of the polymer chains' mobility dominates. This is probably due to the better dispersion of tHNT nanotubes, resulting in higher T_g. Comparison plots of the storage modulus (E') and loss factor (tan δ) are depicted in Fig. 9, as a function of temperature, for LLDPE and related nanocomposites.

The EWF method was applied to characterize the fracture behavior. At first, the basic preconditions necessary for the application of the EWF methodology were verified [53]. In particular, the validity criterion verifies that all tests were conducted under plane-stress state. Furthermore, all the specimens exhibited delayed yielding (i.e., ligament yielding is time dependent and finishes when the crack has already started propagating). However, a relatively brittle behavior is exhibited for the LLDPE-uHNT-8 nanocomposite DEN-T specimen (Fig. 10). The force-displacement curve shows that after yielding, the specimen fails abruptly, showing no stable crack propagation phase. Conversely, the LLDPE-tHNT-8 nanocomposite DEN-T specimen manifests ductile fracture after
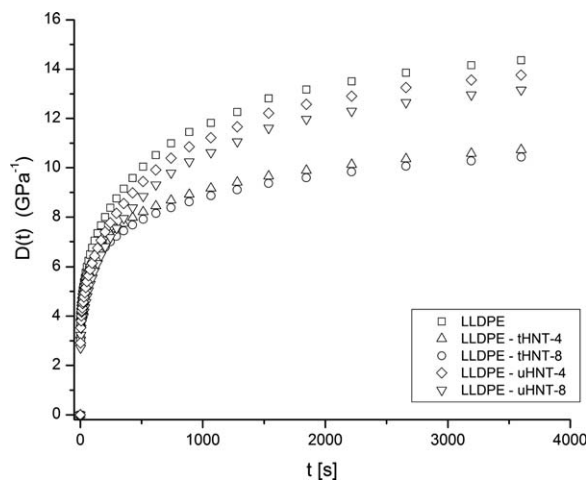
FIG. 8. Creep compliance ($D(t)$) of LLDPE and relative nanocomposites as a function of time ($T = 30°C$, $\sigma_0 = 1$ MPa).

TABLE 5. Creep compliance data and dynamic mechanical properties of LLDPE and relative nanocomposites ($f = 1$ Hz).

Sample	D_e (GPa^{-1})	$D_{ve,2000s}$ (GPa^{-1})	$D_{tot,2000s}$ (GPa^{-1})	E' ($-130°$C; MPa)	E' ($23°$C; MPa)	E'' ($23°$C; MPa)	T_g (°C)
LLDPE	5.96	7.39	13.35	4236	416	26.0	-110.5
LLDPE-uHNT-1	5.85	7.33	13.18	4318	422	50.7	-110.9
LLDPE-uHNT-4	5.62	7.11	12.73	4724	539	56.1	-109.1
LLDPE-uHNT-8	5.55	6.72	12.27	4970	778	59.3	-109.2
LLDPE-tHNT-1	5.80	7.33	13.13	4358	518	49.5	-110.0
LLDPE-tHNT-4	5.56	4.52	10.08	4634	738	62.1	-109.9
LLDPE-tHNT-8	5.46	4.25	9.71	5094	813	66.8	-109.1

D_e: Elastic creep compliance.
$D_{ve,2000s}$: Viscoelastic creep compliance at 2000 s.
$D_{tot,2000s}$: Total creep compliance at 2000 s.
E' ($-130°$C): Storage modulus at $-130°$C.
E' ($23°$C): Storage modulus at $+23°$C.
E'' ($23°$C): Loss modulus at $+23°$C.
T_g: Glass transition temperature as recorded in *tan δ* peak.

yielding. As already observed by Mouzakis et al. when investigating the fracture toughness in both syndiotactic and isotactic PP filled with multiwall CNTs, the ideal necking-yielding-stable neck tearing sequence, is usually desired for the application of the EWF approach in DEN-T specimens [73].

In particular, in all LLDPE-tHNT nanocomposites, the area under the curve after the maximum force was reached is higher than that prior to maximum force, indicating stable crack propagation with high energy absorption, typical of ductile materials [49] (Fig. 11A). This is a clear indication that the addition of tHNT
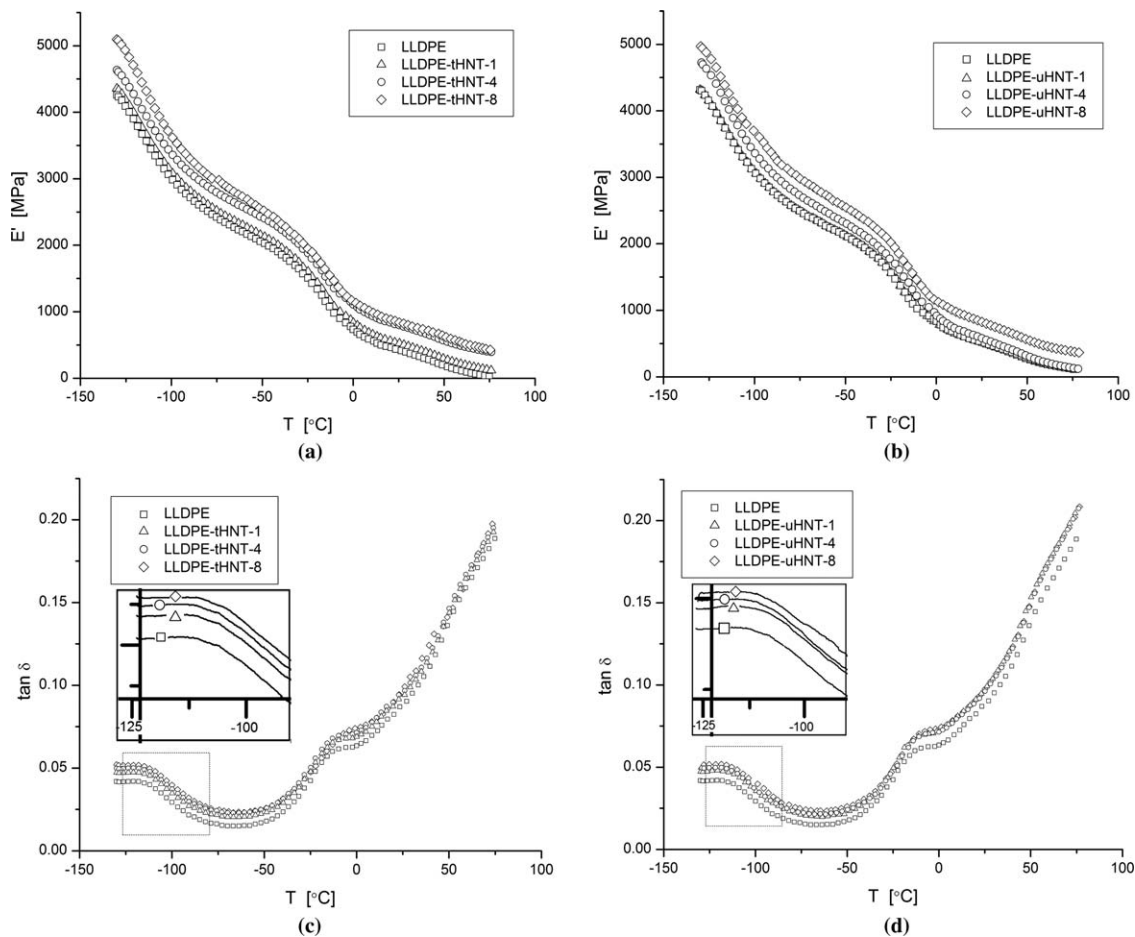
FIG. 9. DMA properties of LLDPE and its HNT nanocomposites ($f = 1$ Hz): (a and b) Storage modulus (E') and (c and d) Loss tangent (*tan δ*) as a function of temperature.
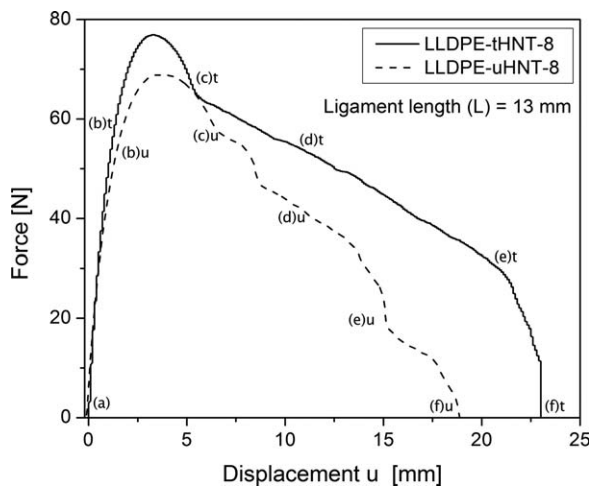
FIG. 10. Typical force-displacement curves recorded for DEN-T specimens of LLDPE-tHNT-8 and LLDPE-uHNT-8 during the EWF tests. Each characteristic point, as indicated on the curve with a letter, corresponds to the relative picture reported in Fig. 11.

improves the strength of LLDPE without embrittlement of the material.

The elliptical shape of the stress-whitened zone (characterized by a shape factor β) formed during tensile EWF

test performed on LLDPE nanocomposites was similar to that of neat LLDPE with slight variation in the height of the zone. The total specific EWF, the specific EWF at yielding and the specific EWF for necking were obtained by linear fits and tabulated in Table 6. A huge improvement (up to a factor of 2) in w_e is noticed as the tHNT content increases, whereas βw_p values slightly decrease on filler addition. These results indicate that tHNT addition significantly toughened the matrix [49].

Moreover, partitioned components of total EWF, such as EWF for yielding ($w_{e,y}$) and EWF for necking ($w_{e,n}$), also show an improvement in all nanocomposites when compared to unfilled LLDPE. In particular, the improvement in $w_{e,y}$ is probably due to the higher yield stress recorded for nanocomposites with respect to LLDPE while the change in $w_{e,n}$ might be because of changes in the crack propagation behavior in the nanocomposites [74].

Conversely, LLDPE-uHNT composites show higher w_e only at 1 and 4 wt% concentrations, while the sample LLDPE-uHNT-8 manifests lower toughness showing smaller w_e than unfilled LLDPE. Furthermore, the component $w_{e,y}$ is very high, while $w_{e,n}$ appears quite low compared to other nanocomposites. This indicates that most of the deformation energy is spent for yielding, while
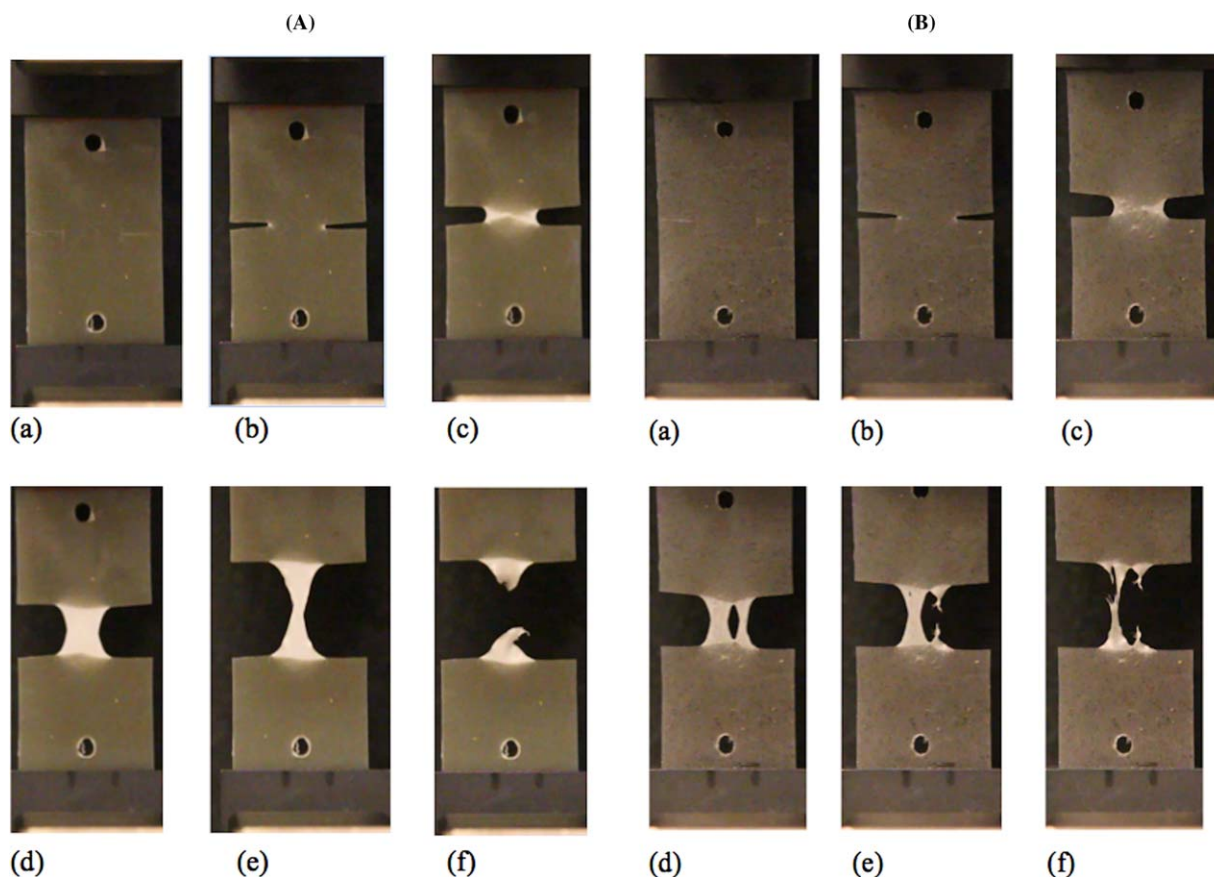
FIG. 11. Serial photographs taken from the DEN-T specimens of the nanocomposites (A) LLDPE-tHNT-8 and (B) LLDPE-uHNT-8 during the EWF tests at different times ($L = 13$ mm). [Color figure can be viewed in the online issue, which is available at wileyonlinelibrary.com.]

TABLE 6. Specific EWF properties of LLDPE and relative nanocomposites.

Sample	w_e (kJ/m^2)	$\beta\, w_p$ (MJ/m^3)	β	$w_{e,y}$ (kJ/m^2)	$\beta'\, w_{p,y}$ (MJ/m^3)	$w_{e,n}$ (kJ/m^2)	$\beta''\, w_{p,n}$ (MJ/m^3)
LLDPE	26.7 ± 3.6	12.7 ± 0.4(0.983)	0.32 ± 0.04	2.7 ± 0.3	2.8 ± 0.1(0.997)	24.2 ± 3.6	9.9 ± 0.4(0.992)
LLDPE-uHNT-1	29.4 ± 3.4	12.0 ± 0.4(0.984)	0.31 ± 0.03	3.3 ± 0.5	2.7 ± 0.1(0.994)	26.1 ± 3.4	9.3 ± 0.4(0.989)
LLDPE-uHNT-4	38.1 ± 1.9	8.7 ± 0.2(0.990)	0.30 ± 0.04	6.6 ± 0.5	2.2 ± 0.1(0.990)	31.5 ± 2.0	6.5 ± 0.2(0.991)
LLDPE-uHNT-8	21.8 ± 2.3	12.2 ± 0.3(0.992)	0.26 ± 0.05	8.8 ± 0.5	2.1 ± 0.1(0.983)	13.0 ± 2.4	10.1 ± 0.3(0.988)
LLDPE-tHNT-1	29.0 ± 3.0	12.9 ± 0.3(0.988)	0.29 ± 0.06	3.7 ± 0.5	2.2 ± 0.1(0.986)	25.3 ± 3.0	10.7 ± 0.3(0.990)
LLDPE-tHNT-4	40.4 ± 3.0	10.9 ± 0.3(0.984)	0.25 ± 0.05	6.4 ± 0.7	1.8 ± 0.1(0.964)	34.0 ± 3.1	9.1 ± 0.3(0.991)
LLDPE-tHNT-8	55.0 ± 1.3	6.4 ± 0.2(0.992)	0.26 ± 0.03	6.5 ± 0.4	1.6 ± 0.1(0.986)	48.5 ± 1.4	4.8 ± 0.2(0.988)

w_e: Specific essential work of fracture.

$\beta\, w_p$: Specific nonessential work of fracture.

β: Shape factor (taking into account an elliptical shape of the plastic zone).

$w_{e,y}$: Specific essential work of fracture for yielding.

$\beta'\, w_{p,y}$: Specific nonessential work of fracture for yielding.

$w_{e,n}$: Specific essential work of fracture for necking.

$\beta''\, w_{p,n}$: Specific nonessential work of fracture for necking.

The values in brackets correspond to R^2 values obtained from the linear regression of the data.

very low amount of energy contributes to necking. Moreover, the β factor appears lower than that of the other LLDPE-uHNT samples, indicating a clear reduction in the height of the deformation zone. Although the related specimens exhibit delayed yielding, the plastic deformation zone, formed by crazing, is highly constrained. The latter yields restricted necking during the subsequent deformation (Fig. 11B). This behavior clearly indicates that the addition of uHNT at 8 wt% is associated with reinforcing effect and, concurrently, with a prominent loss in ductility. This feature is in accordance with the results of the quasi-static tensile tests.

When the load is applied at high strain rates such as under impact conditions, the introduction of tHNT nanoparticles leads to an increase of the energy adsorbed at break (TEB; Table 7). This is in line with the TEB$_{qs}$ data reported in quasi-static tensile tests (Table 4). Conversely, the addition of uHNT produces a slight decrease in TEB, proportional to the filler content. This is most likely due to extensive filler agglomeration and poor matrix/filler interfacial interaction. The enhancement in impact strength, found for LLDPE-tHNT specimens, can be ascribed to the beneficial effects of the well-dispersed tHNT nanotubes. The latter are obviously triggering failure events linked with HNT

debonding, pull-out and breakage phenomena. [20, 37, 75, 76]. Moreover, the crystallization of the polymer with the addition of the filler may affect the toughness, as well (Table 2). The better dispersion tHNT (based on SEM and TEM investigations) and the surface treatment (leading to better interfacial interaction) are further factors, which may be responsible for the observed improvement found for LLDPE-tHNT compared to LLDPE-uHNT nanocomposites.

CONCLUSIONS

The addition of treated nanoparticles resulted in a better dispersion of the filler within the matrix, as confirmed by SEM and TEM observations. HNT nanotubes acted as a weak nucleating agent, producing an increase of the crystallization peak temperature. The melt viscosity of nanocomposites decreased with nanofiller incorporation, showing an interesting feature of practical relevance.

Tensile tests indicated that the nanoparticles can reinforce LLDPE at a low filler content, especially in the case of tHNT, without loss in ductility. Creep tests showed that creep compliance was markedly reduced by nanofiller incorporation, while storage and loss moduli were enhanced in all nanocomposites.

The toughness of the LLDPE-tHNT, evaluated through EWF method, outperformed both the LLDPE matrix and the LLDPE-uHNT nanocomposites. Incorporation of tHNT in 8 wt% increased the fracture toughness of the LLDPE matrix by a factor of about 2.

TABLE 7. Tensile impact properties at break.

Sample	Maximum strength (MPa)	Elongation at break (%)	TEB[a] (J/m^3)
LLDPE	40.2 ± 2.7	135 ± 15	18.9 ± 2.3
LLDPE-uHNT-1	40.0 ± 3.5	121 ± 13	18.0 ± 1.6
LLDPE-uHNT-4	39.3 ± 4.1	95 ± 16	15.2 ± 3.2
LLDPE-uHNT-8	35.3 ± 3.0	89 ± 11	14.4 ± 0.5
LLDPE-tHNT-1	40.2 ± 3.1	155 ± 12	19.4 ± 2.7
LLDPE-tHNT-4	40.8 ± 3.7	142 ± 10	19.3 ± 2.0
LLDPE-tHNT-8	38.2 ± 5.7	129 ± 13	18.7 ± 1.3

[a]Tensile energy to break measured during tensile impact test.

REFERENCES

1. J. Karger-Kocsis and S. Siengchin, *KMUTNB Int. J. Appl. Sci. Technol.*, **7**, 1 (2014).

2. F. Hussain, *J. Compos. Mater.*, **40**, 1511 (2006).

3. S. Fu, X. Feng, B. Lauke, and Y. Mai, *Compos. B*, **39**, 933 (2008).

4. J. Njuguna, K. Pielichowski, and S. Desai, *Polym. Adv. Technol.*, **19**, 947 (2008).

5. J. Jancar, *J. Mater. Sci.*, **43**, 6747 (2008).

6. L.S. Sutherland, R.A. Shenoi, and S.M. Lewis, *Compos. Sci. Technol.*, **59**, 209 (1999).

7. P.-C. Ma, N.A. Siddiqui, G. Marom, and J.-K. Kim, *Compos. A*, **41**, 1345 (2010).

8. A.R. Bhattacharyya, T.V. Sreekumar, T. Liu, S. Kumar, L.M. Ericson, R.H. Hauge, and R.E. Smalley, *Polymer*, **44**, 2373 (2003).

9. J.Y. Kim, *J. Appl. Polym. Sci.*, **112**, 2589 (2009).

10. K. Lau, C. Gu, and D. Hui, *Compos. B*, **37**, 425 (2006).

11. A. Panwar, V. Choudhary, and D.K. Sharma, *J. Reinforced Plast. Compos.*, **30**, 446 (2011).

12. E. Olewnik, K. Garman, and W. Czerwiński, *J. Therm. Anal. Calorim.*, **101**, 323 (2010).

13. P.H. Nam, P. Maiti, M. Okamoto, T. Kotaka, N. Hasegawa, and A. Usuki, *Polymer*, **42**, 9633 (2001).

14. F. Perrin-Sarazin, M.T. Ton-That, M.N. Bureau, and J. Denault, *Polymer*, **46**, 11624 (2005).

15. K. Kalaitzidou, H. Fukushima, and L.T. Drzal, *Carbon*, **45**, 1446 (2007).

16. R. Sengupta, M. Bhattacharya, S. Bandyopadhyay, and A.K. Bhowmick, *Prog. Polym. Sci.*, **36**, 638 (2011).

17. K. Kalaitzidou, H. Fukushima, and L.T. Drzal, *Compos. A*, **38**, 1675 (2007).

18. B. Guo, Q. Zou, Y. Lei, M. Du, M. Liu, and D. Jia, *Thermochim. Acta*, **484**, 48 (2009).

19. B. Lecouvet, J.G. Gutierrez, M. Sclavons, and C. Bailly, *Polym. Degrad. Stab.*, **96**, 226 (2011).

20. K. Prashantha, H. Schmitt, M.F. Lacrampe, and P. Krawczak, *Compos. Sci. Technol.*, **71**, 1859 (2011).

21. N. Abdel-Aal, F. Ei-Tantawy, A. Al-Hajry, and M. Bououdina, *Polym. Compos.*, **29**, 511 (2008).

22. Y.K. Choi, K. Sugimoto, S.M. Song, Y. Gotoh, Y. Ohkoshi, and M. Endo, *Carbon*, **43**, 2199 (2005).

23. C. Gauthier, L. Chazeau, T. Prasse, and J.Y. Cavaille, *Compos. Sci. Technol.*, **65**, 335 (2005).

24. M.A. Tarawneh, S.H. Ahmad, S.Y. Yahya, and R. Rasid, "Effect of ultrasonic treatment on the tensile and impact properties of thermoplastic natural rubber nanocomposites reinforced with carbon nanotubes," in: AIP Proceedings International Conference on Nanoscience and Nano-technology, Nano-SciTech 2008, 18-21 November 2008, Selangor (2009).

25. X.H. Liu and Q.J. Wu, *Polymer*, **42**, 10013 (2001).

26. C.L. Wu, M.Q. Zhang, M.Z. Rong, and K. Friedrich, *Compos. Sci. Technol.*, **62**, 1327 (2002).

27. A. Dorigato, A. Pegoretti, F. Bondioli, and M. Messori, *Compos. Interf.*, **17**, 873 (2010).

28. D.N. Bikiaris, A. Vassiliou, E. Pavlidou, and G.P. Karayannidis, *Eur. Polym. J.*, **41**, 1965 (2005).

29. K. Prashantha, M.F. Lacrampe, and P. Krawczak, *Express Polym. Lett.*, **5**, 295 (2011).

30. P. Blaszczak, W. Brostow, T. Datashvili, and H.E.H. Lobland, *Polym. Compos.*, **31**, 1909 (2010).

31. A. Fernández, M. Muniesa, and J. González, *J. Mech. Eng.*, **59**, 1 (2013).

32. B. Guo, F. Chen, Y. Lei, X. Liu, J. Wan, and D. Jia, *Appl. Surf. Sci.*, **255**, 7329 (2009).

33. D. Rawtani and Y.K. Agrawal, *Rev. Adv. Mater. Sci.*, **30**, 282 (2012).

34. D. Rawtani and Y.K. Agrawal, *Emerg. Mater. Res.*, **1**, 212 (2012).

35. M. Du, B. Guo, and D. Jia, *Polym. Int.*, **59**, 574 (2010).

36. M. Du, B. Guo, M. Liu, and D. Jia, *Polym. J.*, **38**, 1198 (2006).

37. M. Murariu, A.-L. Dechief, Y. Paint, S. Peeterbroeck, L. Bonnaud, and P. Dubois, *J. Polym. Environ.*, **20**, 932 (2012).

38. D.C.O. Marney, L.J. Russell, D.Y. Wu, T. Nguyen, D. Cramm, N. Rigopoulos, N. Wright, and M. Greaves, *Polym. Degrad. Stab.*, **93**, 1971 (2008).

39. E. James, *Polymer Data Handbook*, Oxford University Press, New York (1999).

40. A. Dorigato, A. Pegoretti, and A. Penati, *Express Polym. Lett.*, **4**, 115 (2010).

41. A. Dorigato, Y. Dzenis, and A. Pegoretti, *Procedia Eng.*, **10**, 894 (2011).

42. A. Dorigato, A. Pegoretti, and J. Kolařík, *Polym. Compos.*, **31**, 1947 (2010).

43. A. Dorigato, A. Pegoretti, and Y. Dzenis, *Mech. Mater.*, **61**, 79 (2013).

44. Z. Jia, Y. Luo, B. Guo, B. Yang, M. Du, and D. Jia, *Polym. Plast. Technol. Eng.*, **48**, 607 (2009).

45. A. Dorigato and A. Pegoretti, *Eng. Fract. Mech.*, **79**, 213 (2012).

46. D.E. Mouzakis, G.C. Papanicolaou, C. Argyrakis, G. Kandilioti, D. Kontarinis, and V.G. Gregoriou, *J. Nanostruct. Polym. Nanocompos.*, **4**, 100 (2008).

47. E. Franco-Urquiza, J. Gamez Perez, M. Sánchez-Soto, O.O. Santana, and M.L. Maspoch, *Polym. Int.*, **59**, 778 (2010).

48. M.L. Maspoch, E. Franco-Urquiza, J. Gamez-Perez, O.O. Santana, and M. Sánchez-Soto, *Polym. Int.*, **58**, 648 (2009).

49. T. Bárány, T. Czigány, and J. Karger-Kocsis, *Prog. Polym. Sci.*, **35**, 1257 (2010).

50. D. Pedrazzoli, R. Ceccato, J. Karger-Kocsis, and A. Pegoretti, *Express Polym. Lett.*, **7**, 652 (2013).

51. S. Brunauer, P.H. Emmett, and E. Teller, *J. Am. Chem. Soc.*, **60**, 309 (1938).

52. J. Brandrup, E.H. Immergut, and E.A. Grulke, *Polymer Handbook* (4th edition), Wiley, New York (1999).

53. J.G. Williams and M. Rink, *Eng. Fract. Mech.*, **74**, 1009 (2007).

54. M.H. Shamsi, M. Luqman, F. Basarir, J.-S. Kim, T.-H. Yoon, and K.E. Geckeler, *Polym. Int.*, **59**, 1492 (2010).

55. P. Pasbakhsh, H. Ismail, M.N. Ahmad Fauzi, and A. Abu Bakar, "Halloysite Nanotubes as a Novel Nanofiller for Polymer Nanocomposites," in: 21st Australian Clay Minerals Conference, August 2010, Brisbane (2010).

56. M. Zhao and P. Liu, *J. Therm. Anal. Calorim.*, **94**, 103 (2008).

57. R.L. Frost, O.B. Locos, J. Kristof, and J.T. Kloprogge, *Vib. Spectrosc.*, **26**, 33 (2001).

58. M. Abdel-Goad and P. Pötschke, *J. Non-Newtonian Fluid Mech.*, **128**, 2 (2005).

59. P. Cassagnau, *Polymer*, **49**, 2183 (2008).

60. M. Ganß, B.K. Satapathy, M. Thunga, R. Weidisch, P. Pötschke, and D. Jehnichen, *Acta Mater.*, **56**, 2247 (2008).

61. C. Renger, P. Kuschel, A. Kristoffersson, B. Clauss, W. Oppermann, and W. Sigmund, *J. Eur. Ceram. Soc.*, **27**, 2361 (2007).

62. A.S. Sarvestani, *Eur. Polym. J.*, **44**, 263 (2008).

63. M. Sepehr, L.A. Utracki, X. Zheng, and C.A. Wilkie, *Polymer*, **46**, 11569 (2005).

64. D. Wu, L. Wu, L. Wu, and M. Zhang, *Polym. Degrad. Stab.*, **91**, 3149 (2006).

65. V.M. Khumalo, J. Karger-Kocsis, and R. Thomann, *Express Polym. Lett.*, **4**, 264 (2010).

66. M. Liu, B. Guo, M. Du, F. Chen, and D. Jia, *Polymer*, **50**, 3022 (2009).

67. M. Du, B. Guo, and D. Jia, *Eur. Polym. J.*, **42**, 1362 (2006).

68. A. Dorigato, A. Pegoretti, and A. Frache, *J. Therm. Anal. Calorim.*, **109**, 863 (2012).

69. Y. Dzenis, *Mech. Compos. Mater.* **22**, 14 (1986).

70. M.P. Lourenço, C. de Oliveira, A.F. Oliveira, L. Guimarães, H.A. Duarte, *J. Phys. Chem. C*, **116**, 9405 (2012).

71. L. Guimarães, A.N. Enyashin, G. Seifert, and H.l.A. Duarte, *J. Phys. Chem. C*, **114**, 11358 (2010).

72. J. Kolarik and A. Pegoretti, *Polymer*, **47**, 346 (2006).

73. D.E. Mouzakis, G.C. Papanicolaou, K. Giannadakis, and I. Zuburtikudis, *Strain*, **49**, 348 (2013).

74. J. Karger-Kocsis, V. Khumalo, T. Bárány, L. Mészáros, and A. Pegoretti, *Compos. Interf.*, **20**, 395 (2013).

75. C. Liu, Y.F. Luo, Z.X. Jia, B.C. Zhong, S.Q. Li, B.C. Guo, and D.M. Jia, *Express Polym. Lett.*, **5**, 591 (2011).

76. Y. Lin, K.M. Ng, C.M. Chan, G. Sun, and J. Wu, *J. Colloid Interface Sci.*, **358**, 423 (2011).